

Transition-Metal Dissolution from NMC-Family Oxides: A Case Study

Hannah R. Morin, Donald G. Graczyk, Yifen Tsai, Susan Lopykinski, Hakim Iddir, Juan C. Garcia, Nancy Dietz Rago, Stephen Trask, LeRoy Flores, Seoung-Bum Son, Zhengcheng Zhang, Noah M. Johnson, and Ira Bloom*



Cite This: *ACS Appl. Energy Mater.* 2020, 3, 2565–2575



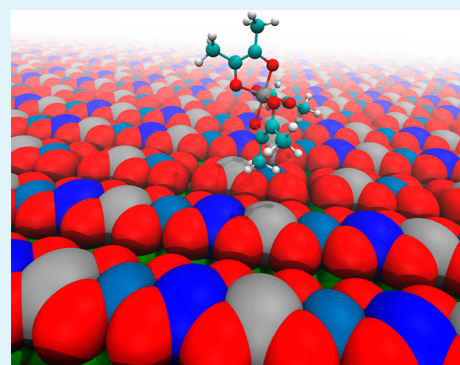
Read Online

ACCESS |

Metrics & More

Article Recommendations

ABSTRACT: We investigated the static reactions of highly delithiated Li-(Ni_{1/3}Mn_{1/3}Co_{1/3})O₂, Li(Ni_{0.5}Mn_{0.3}Co_{0.2})O₂, Li(Ni_{0.6}Mn_{0.2}Co_{0.2})O₂, and Li-(Ni_{0.8}Mn_{0.1}Co_{0.1})O₂ positive electrodes with 2,3-butanedione and with tetrabutyl ammonium bifluoride as model leaching agents. In the bifluoride trials, it was found that [Ni] in the leachate was proportional to $X_{\text{Co}}(X_{\text{Ni}})^3$, where X_{M} is the ideal stoichiometry in the bulk oxide, and inversely proportional to $(X_{\text{Mn}})^2$; [Mn] to $X_{\text{Co}}(X_{\text{Ni}})$; and [Co] to X_{Co} . The relationships between metal concentrations and stoichiometry may indicate that nickel, as a next-nearest neighbor on the positive electrode surface, can make dissolution more favorable in some instances.



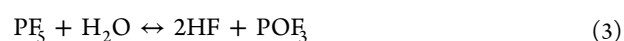
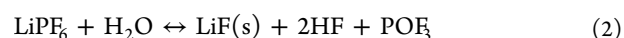
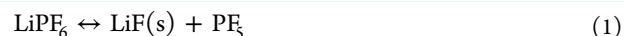
KEYWORDS: lithium-ion battery, metal dissolution, positive electrode materials, kinetics, corrosion by HF, corrosion by electrolyte decomposition

1. INTRODUCTION

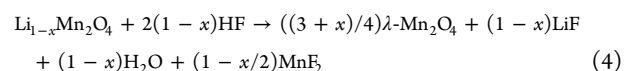
Lithium-ion cells are being considered for automotive applications because of their desirable combination of high specific energy and power. The potential driving range is determined by the amount of energy stored in the cell. Increasing the energy stored would, therefore, increase the driving range of a pure electric vehicle powered by these cells. There are many strategies to increase the energy stored, such as charging the cell to higher voltages. However, voltages higher than about 4.2–4.3 V also increase the performance degradation rate with cycling. At this high voltage, the positive electrode is more delithiated than at lower voltages, making the positive electrode susceptible to attack by corrosive agents, such as those from electrolyte decomposition.

There is much anecdotal evidence in the literature on the effect of electrolyte decomposition products on positive electrode leaching. Usually, the evidence has been derived by taking aged cells apart and determining the concentrations of transition metals in the residual electrolyte or in the anode. There was very little direct evidence of the nature of the agent that caused the change. Most of the reports in the literature cite possible HF as the key factor that was responsible for metal migration from LiMn₂O₄ and Li(Ni_xMn_yCo_{1-x-y})O₂ positive electrode materials.

Hydrofluoric acid can form from the decomposition of the LiPF₆ salt and residual water in the electrolyte, as shown in eqs 1–3.^{1,2}



The presence of HF has been combined with the mechanism that Hunter proposed in his synthesis of λ -MnO₂³ to rationalize the migration of manganese from LiMn₂O₄ positive electrode materials, as shown in eq 4.^{4–8}



It should be noted that the disproportionation reaction of Mn³⁺, $2\text{Mn}^{3+} \leftrightarrow \text{Mn}^{4+} + \text{Mn}^{2+}$ ^{4–8} is key to eq 4. Here, the Mn²⁺ species would be soluble in the electrolyte and could migrate to the anode. The presence of Mn at the anode has been correlated with capacity fade.^{5–11}

Aoshima et al. proposed that the manganese reduction mechanism involves the decarboxylation of organic carbonates catalyzed by the nascent λ -MnO₂. The product of this reaction,

Received: November 21, 2019

Accepted: February 7, 2020

Published: February 7, 2020

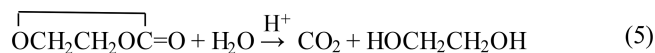
for example, ethanol from diethyl carbonate, then reduces Mn^{4+} to Mn^{2+} . The resulting species then react further to yield soluble manganese fluorophosphates, which, in turn, are free to migrate across the cell.¹¹

Transition-metal dissolution and migration have been seen with other positive electrode materials, such as those based on lithium nickel–manganese–cobalt oxides (NMC), e.g., $\text{Li}(\text{Ni}_{0.5}\text{Mn}_{0.3}\text{Co}_{0.2})\text{O}_2$. Here, high cell voltages (>4.3 V) were correlated with increased concentrations of transition metals in the anode.^{7,9} The concentrations of Ni, Mn, and Co from $\text{Li}(\text{Ni}_{0.5}\text{Mn}_{0.3}\text{Co}_{0.2})\text{O}_2$ positive electrodes in graphite anodes increased proportionately with cell voltage.

Gallus et al.¹² and Zheng et al.⁹ showed that the nature of the salt is important for transition-metal dissolution to occur in NMC materials. Using LiPF_6 , LiClO_4 , and LiBF_4 , Gallus et al. showed that the amount of metal dissolution followed the general trend $\text{LiBF}_4 > \text{LiPF}_6 > \text{LiClO}_4$, which may be related to the stability of the salt against hydrolysis and the voltage range in which it is stable.

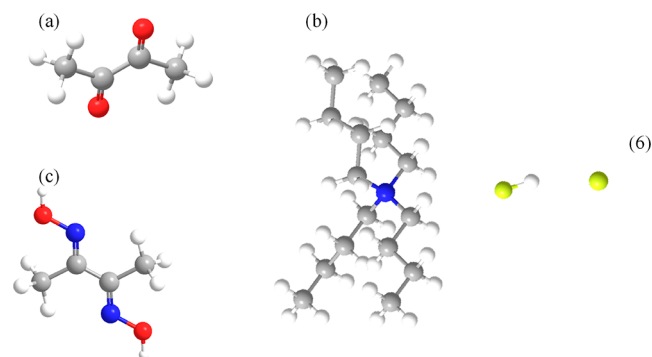
Hydrofluoric acid is not the only possible leaching agent that could be in the cell. Species derived from the decomposition/reaction of the organic electrolyte components could also act. Jarry et al. have proposed that β -diketones or diketones, which form at the charged positive electrode surface, could also facilitate the dissolution of transition metals.¹³ Gilbert et al. suggested that acetates formed from electrolyte decomposition could also play a part.¹⁴

Ethylene carbonate, in theory, may undergo acid-catalyzed de-esterification by reacting with a trace amount of acid in the presence of residual water (eq 5).⁷ At the charged positive



electrode, the nascent ethylene glycol could be oxidized to glyoxal, $\text{CH}(\text{=O})\text{CH}(\text{=O})$, using the principles outlined by Aoshima et al.¹¹ Either ethylene glycol or glyoxal could facilitate metal dissolution.

We investigated the static reactions of $\text{Li}(\text{Ni}_{1/3}\text{Mn}_{1/3}\text{Co}_{1/3})\text{O}_2$ (NMC111), $\text{Li}(\text{Ni}_{0.5}\text{Mn}_{0.3}\text{Co}_{0.2})\text{O}_2$ (NMC532), $\text{Li}(\text{Ni}_{0.6}\text{Mn}_{0.2}\text{Co}_{0.2})\text{O}_2$ (NMC622), and $\text{Li}(\text{Ni}_{0.8}\text{Mn}_{0.1}\text{Co}_{0.1})\text{O}_2$ (NMC811) positive electrodes with two candidate corrosive agents: 2,3-butanedione (biacetyl, eq 6a) and tetrabutyl



ammonium bifluoride ($(\text{C}_4\text{H}_9)_4\text{NF} \cdot \text{HF}$, eq 6b). Structural depictions of these materials are shown in eq 6, where the gray spheres are carbon atoms; white, hydrogen; red, oxygen; yellow, fluorine; and blue, nitrogen.¹⁵

Biacetyl was used instead of glyoxal because both ethylene glycol and glyoxal are difficult to obtain in the pure state.¹⁶ Additionally, biacetyl would be expected to be selective for Ni.

It is structurally similar to dimethyl glyoxime (eq 6c), which is used in analytical chemistry to test for the presence of Ni^{2+} , forming a brilliant red precipitate.^{17–20} The bifluoride salt was used because it is an organically soluble source of HF. The positive electrode materials were charged to 4.6 V in full cells, producing highly delithiated materials that should be very susceptible to attack. The positive electrodes were placed in a small amount of electrolyte solvent containing the agent of interest and allowed to stand at room temperature for 6 days. The amounts of Mn, Co, and Ni in the solvent were determined by inductively coupled plasma-mass spectrometry (ICP-MS). Theoretical calculations were performed to aid the understanding of the ICP-MS data.

2. METHODS

2.1. Materials. Battery-grade ethylene carbonate (EC), ethyl methyl carbonate (EMC) (Sigma-Aldrich or Tomiyama Chemicals, Inc.), 2,3-butanedione (Alfa-Aesar), and tetrabutylammonium bifluoride (95%, Tokyo Chemicals, Inc.) were used as received. The Celgard 2325 separator was used as received. The separator was cut into 16-mm-diameter disks.

Single-sided electrode laminates of the positive and negative electrode materials were made at Argonne's CAMP²¹ Facility. Their compositions are given in Table 1. All positive electrode and anode laminates were made in a dry room (dewpoint: -40 °C maximum). These electrode couples were designed to be cycled between 3 and

Table 1. Laminate Compositions Used in This Work

anode laminate (used in all experiments)
91.83 wt % Phillips66 CPreme A12 graphite
2 wt % Timcal C45 carbon
6 wt % Kureha 9300 poly(vinylene difluoride) (pVdF) binder
0.17 wt % oxalic acid
coating thickness: 43 μm (6.07 mg cm^{-2} ; 34.9% porosity)
Cu foil thickness: 10 μm
NMC111
90 wt % Toda NMC111 (powder surface area = $0.44 \text{ m}^2 \text{ g}^{-1}$; $D_{50} = 8.6 \mu\text{m}$)
5 wt % Timcal C-45 carbon
5 wt % Solvay S130 pVdF binder
coating thickness: 41 μm (11.22 mg cm^{-2} ; 33.5% porosity)
Al foil thickness: 20 μm
NMC532
90 wt % Toda NMC532 (powder surface area = $0.32 \text{ m}^2 \text{ g}^{-1}$; $D_{50} = 9.3 \mu\text{m}$)
5 wt % Timcal C45 carbon
5 wt % Solvay S130 pVdF
coating thickness: 34 μm (9.12 mg cm^{-2} ; 33.9% porosity)
Al foil thickness: 20 μm
NMC622
90 wt % EcoPro NMC622 (powder surface area = $0.20 \text{ m}^2 \text{ g}^{-1}$; $D_{50} = 11.0 \mu\text{m}$)
5 wt % Timcal C45 carbon
5 wt % Solvay S130 pVdF
coating thickness: 41 μm (10.03 mg cm^{-2} ; 35.5% porosity)
Al foil thickness: 20 μm
NMC811
90 wt % Targray NMC811 (powder surface area = $0.40 \text{ m}^2 \text{ g}^{-1}$; $D_{50} = 13.2 \mu\text{m}$)
5 wt % Timcal C45 carbon
5 wt % Solvay S130 pVdF
coating thickness: 32 μm (8.34 mg cm^{-2} ; 36.3% porosity)
Al foil thickness: 20 μm

4.2 V. The negative/positive (N/P) capacity ratios are given in Table 2.

Table 2. N/P Ratio as a Function of Cycling Voltage Range, Based on C/10 Capacities

positive electrode material	voltage range	
	3.0 to 4.2 V	3.0 to 4.6 V (estimate)
NMC111	1.21 to 1.30	0.81 to 0.95
NMC532	1.36 to 1.46	1.02 to 1.14
NMC622	1.20 to 1.26	0.89 to 0.96
NMC811	1.34 to 1.41	1.06 to 1.19

The positive and negative electrode laminates were cut into 14- and 15-mm-diameter disks, respectively, in air. After drying the electrodes overnight at 70 °C in vacuo, the solid cell components were assembled into 2032-sized coin cells in an argon-filled glovebox. The electrolyte, consisting of 1.2 M LiPF₆ in EC/EMC (3:7 by weight), was added. The electrodes were flooded with electrolyte.

The cells were charged with a MACCOR 4000 battery tester. The testing schedule included an initial charge at the C/3 rate to 1.5 V, followed by a 9 h rest. The cell was charged at the C/20 rate to 4.6 V and held at that voltage until the measured current was less than the C/200 rate. The N/P ratios at the higher voltage were lower; these values are also shown in Table 2.

In the glovebox, the cells were opened and the positive electrodes were harvested. Each positive electrode was washed with excess anhydrous dimethyl carbonate (Sigma-Aldrich) two times, swirling for 1 min each time.

2.2. Leaching Experiment. All trials were performed at least twice. For a given experiment, a series of 7 mL perfluoroalkoxy plastic (PFA) vials and caps (Saville) were used. The threads of each vial were wrapped with a layer of Teflon tape to create a vapor-resistant seal.

The cleaned positive electrode disks were placed in the vials along with 1 mL of EC/EMC (3:7 by weight). Metered amounts of 2,3-butanedione (0 to 50 μ L) were added using an Eppendorf pipet. After being sealed with the matching PFA lids, the vials were allowed to stand at room temperature for 6 days in the glovebox.

In separate trials, tetrabutyl ammonium bifluoride, Bu₄NF·HF, was added. Amounts ranged from 0 to 100 mg because the reagent was extremely viscous and difficult to dispense reproducibly. The operations involving the bifluoride reagent were carried out in an argon-purged glovebag. (Note that Bu₄NF·HF is extremely hygroscopic.) (*Caution! Bu₄NF·HF should be handled as if it were HF.*) All solutions were exposed to the glovebag atmosphere, even those to which no bifluoride was added. The vials were sealed and allowed to

stand for 6 days at room temperature in an argon-purged, sealed Nalgene bottle.

The products of the reactions were handled in air. The product liquid was harvested using a plastic pipet (Molecular Bio Products, San Diego, CA) and was filtered using a 25-mm-diameter, 0.2 μ m poly(tetrafluoroethylene) filter (Fischer Scientific) attached to a 1 mL polypropylene syringe (NormJect). The filtered liquid was collected in a 2 mL Nalgene cryogenic vial (Thermo Scientific) and sealed.

2.3. Elemental Analysis. Weighed amounts of each product liquid were placed in clean centrifuge tubes. Over 3 days, the liquid in the open tubes was evaporated in a clean hood to a minimum volume. Then, 2 mL of reagent water was added, the solution was mixed, and 0.2 mL of Optima grade nitric acid was added. This mixture was diluted with reagent water to a final volume of 10 mL.

The Ni, Co, and Mn concentrations in the resulting mixtures were measured with a PerkinElmer NexION 2000 ICP mass spectrometer calibrated with standards prepared from NIST traceable solutions. The corrosion data were obtained from the measured ICP-MS data, the volume of the prepared solution, and the mass or volume of the sample taken. The uncertainties in the reported corrosion values represent the standard deviation of the measurements. If the reported values were the same, then the uncertainty was set at $\pm 10\%$.

The concentrations of fluoride were determined with an ion-selective electrode. Fluoride was determined using a Thermo Scientific Orion Star A214 meter with a combination fluoride-ion selective electrode, model 9609BNWP.

A direct calibration technique was used for analysis of the samples wherein the concentration of a sample was determined by comparison to standards. The meter was standardized with a two-point calibration using 1 and 10 μ g mL⁻¹ fluoride standards. Both standards contained total ionic strength adjustment buffer (TISAB II). After calibration, the 1 μ g mL⁻¹ fluoride standard was used as a check. Samples were diluted 1:1 with TISAB II. Standards and samples were monitored for temperature and stirred at a uniform rate during analysis.

2.4. X-ray Diffraction and Microscopy. X-ray diffraction (XRD) patterns of pristine and delithiated positive electrode laminates were obtained with a Bruker D8 Advance diffractometer in the 2θ range of 10–80° using monochromatic Cu K α radiation. During analysis, 14 mm disks of positive electrode laminates were held in place and protected from air by a layer of Kapton tape. GSAS²² was used to perform Rietveld refinement on the XRD data, producing values of the lattice constants.

The laminates were cut with a razor blade. Scanning electron microscopy (SEM) of cross sections of the laminates was performed using a JEOL JSM6610LV scanning electron microscope. The micrographs were obtained using 10 kV accelerating voltage and a working distance of 20 mm.

2.5. Atomistic Modeling. Atomistic simulations were carried out using a spin-polarized density functional theory (DFT) calculations as

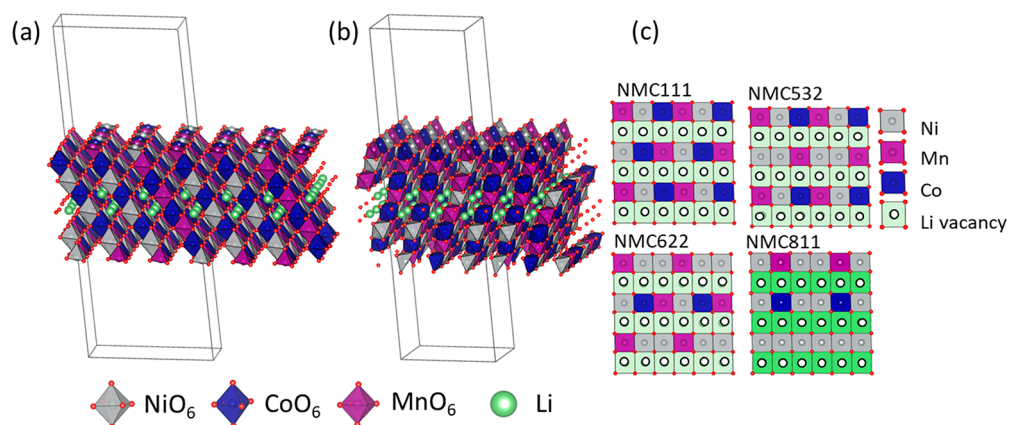


Figure 1. Schematic representation of the charged NMC111 slab model surface for (a) facet (104) and (b) facet (012). (c) Top view of the surfaces for the four studied compositions.

implemented in the Vienna ab initio simulation package (VASP).^{23,24} The exchange-correlation potentials were treated with the generalized gradient approximation (GGA) parametrized by Perdew, Burke, and Ernzerhof (PBE).²⁵ The interactions between valence electrons and ion cores were described by the projected augmented wave (PAW) method.²⁶ All of the ions were allowed to relax until the total energy differences were no more than 0.003 eV.

The energy needed to form a complex using a transition metal from the surface was calculated using a slab model with 12 Å vacuum space (see Figure 1). Surface facets (104) and (012) were simulated because they have been found to be the most predominant in NMC positive electrodes.²⁷ Each slab has 8 layers, formed by transition metals and Li ions in octahedral sites, containing a total of 72 transition-metal ions. The first three layers are delithiated in order to simulate a charged positive electrode. An implicit solvation model was used to describe the interactions between the metal complex and the solvent, as implemented in DFT code VASP.^{28,29} The dielectric constant for this continuum medium was chosen to be 18.5, as recommended for an EC/EMC (3:7 by weight) binary mixture at room temperature.³⁰

2.6. Data Reduction. The charging capacity data for each cell were taken directly from the MACCOR files. The values from the constant-current and constant-voltage portions of charging were summed. Averages and standard deviations were calculated for each positive electrode material by using Microsoft Excel. The concentration values reported below represent the averages of 8 to 10 samples using the additive and the average of two without the additive.

Relationships in the data were determined with Visual Basic for Applications in Excel. We implemented a search algorithm to test all possible combinations of the terms shown in eq 7,

$$[\text{TM}] = b(X_{\text{Mn}})^{\alpha}(X_{\text{Ni}})^{\beta}(X_{\text{Co}})^{\gamma} + C \quad (7)$$

where [TM] is the concentration of either Ni, Mn, or Co in solution; b and C are constants; X_{TM} is the bulk stoichiometry of Mn, Ni, or Co; and α , β , and γ are the orders of the reaction in that component. If the component accelerated the reaction, then the corresponding exponent was positive; if it inhibited the reaction, then the exponent was negative. If α , β , or γ was zero, then there was no contribution from that component to the overall expression.

The actual fitting was performed with the LINEST function in Excel. We restricted the values of α , β , and γ to integers of between -5 and 5 and $|\alpha + \beta + \gamma| \leq 5$. These restrictions arose from a consideration of the surface of the oxide, that is, how many next-nearest-neighbor atoms were transition metals. As shown in Figure 2, each metal center has, at most, five next-nearest-neighbor transition-metal atoms, which limited the range of values possible for the given exponent. A fit was considered acceptable if the regression coefficient, r^2 , was greater than or equal to 0.95.

3. RESULTS

Figure 3 shows cross sections of the pristine laminates, showing their overall microstructures. The microstructure consisted of porous, secondary particles in a porous structure. In some cases, the carbon additive, C45, was also seen as an amorphous-looking material. The extent that the binder covered each primary/secondary particle could not be ascertained from these or other, higher-magnification images. Thus, the reactive area may be proportional to that given in Table 1, but the exact amount is not known.

Figure 4 shows typical charging curves for the four electrode types. There was not much difference in the voltage response with lithium (capacity) removed from the positive electrode. The amount of capacity removed was proportional to the active material loading densities: 2.28, 2.50, 2.07, and 2.81 mAh cm⁻², respectively, for NMC532, NMC622, NMC811, and NMC111. The extent of delithiation for each positive

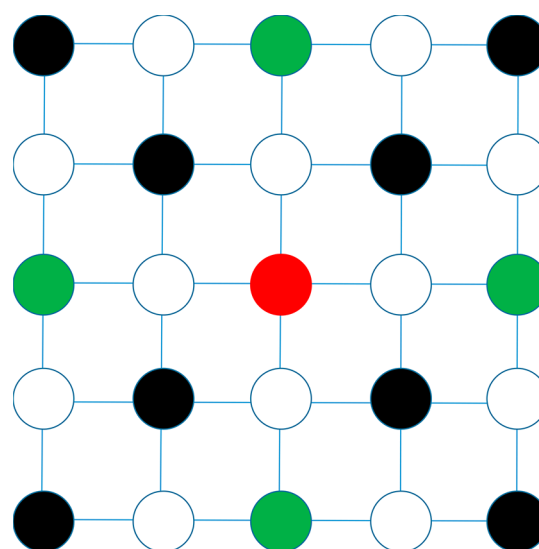


Figure 2. Simplified schematic of a fraction of the oxide surface. The empty circles represent oxygen atoms; the filled ones, transition-metal ions. The red circle has four next-nearest neighbors in this drawing. The number of next-nearest neighbors is five, when one includes the layers beneath the surface. On the surface, there can be oxygen atoms on top of the metals; they were omitted for the sake of clarity. The lithium atoms were excluded from this drawing.

electrode was calculated from the charging data. These results are given in Table 3 and show that all of the positive electrode materials were between 77 and 88% delithiated. The extent of delithiation was lower for NMC111 and NMC622 as compared to the other two materials due to the lower N/P ratio in these cells, most likely resulting in anode polarization and the premature end of cell charging. Even though lithium plating would be expected in these cells, it was not observed.

XRD patterns of the delithiated materials were obtained to verify that the $R\bar{3}m$ crystal structure was still intact. Typical XRD patterns after delithiation are shown in Figure 5. The lattice constants, shown in Table 3, were calculated from these data. Similar values from the pristine materials are also given for reference. The XRD patterns show very little variation, indicating that the same crystal structure was present in all materials, and no obvious second phases were present.

The data in Table 4 show the effect of extensive delithiation on the crystal structure. The lattice constant, a , tends to decrease upon delithiation. However, the lattice constant, c , displays unusual behavior. In NMC111, there is a net increase in c , while for the other positive electrode materials, there is a decrease. This type of behavior has been reported in the literature as being due to a phase change between two hexagonal phases, H2 and H3.^{31,32}

3.1. Biacetyl. The variation in the concentration of transition metals when biacetyl is added is shown in Table 5 for the four positive electrode materials. The net effect of the additive on the concentration of transition metals was calculated using these data. From the data in Table 5, only nickel displayed a statistically significant dependence on the additive in two cases, NMC111 and NMC532. Even though the remaining values shown in Table 5, at first glance, indicate a significant difference above the background, a close examination of the uncertainty in these values indicates that this was not the case. The large uncertainty in some of the values in Tables 4 and 5 makes it very difficult to conclude that

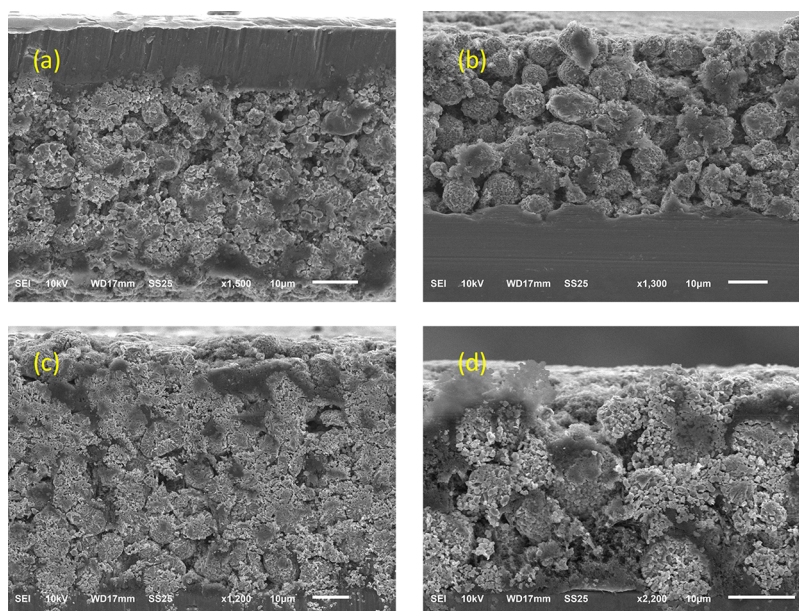


Figure 3. SEM micrographs of cross sections of the laminates: (a) NMC111, (b) NMC532, (c) NMC622, and (d) NMC811. The magnification was adjusted so that the entire laminate thickness could be seen at once. In most cases, the aluminum foil was on the bottom of the photograph; it was on the top in (a).

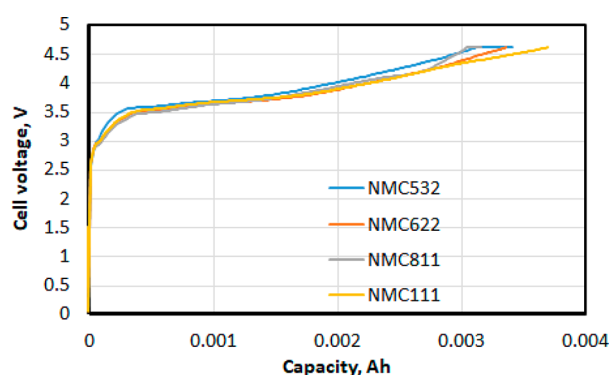


Figure 4. Cell voltage vs capacity during charging of the four positive electrode types.

Table 3. Extent of Delithiation Based on Theoretical Amount of Lithium Available in the Positive Electrode Material

positive electrode	% delithiation (s.d.)
NMC111	77.33 (0.86)
NMC532	83.26 (2.80)
NMC622	81.10 (1.33)
NMC811	87.63 (1.67)

the values were statistically different from zero. That is, they were not significantly different from the background reaction. Therefore, no fitting was performed to generate a model.

The very sharp drop in the concentration of nickel as the nickel fraction increased in the solids seemed counterintuitive. Ordinarily, one would expect that the concentration of nickel in solution would increase with increasing amounts of nickel in the solid.

Atomistic modeling was performed to help us understand these observations. The calculations did not allow surface reconstruction. The composition of the model surface was the same as that of the bulk, and the metal complex was the same

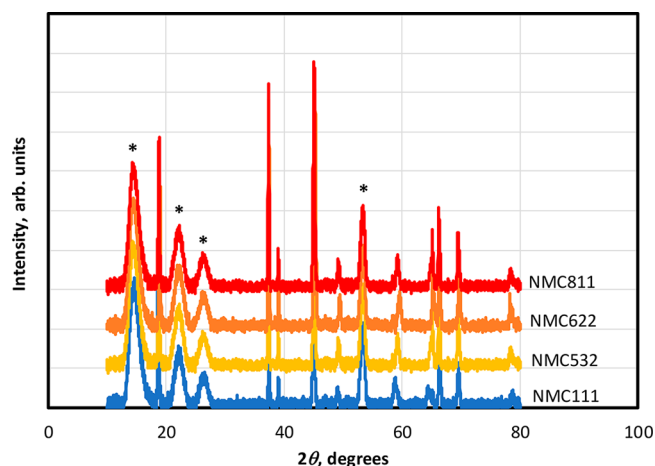


Figure 5. XRD patterns from delithiated positive electrode materials using Cu K α radiation. The peaks marked with an asterisk (*) are from Kapton tape and the sample holder.

Table 4. Lattice Constants ($R\bar{3}m$ Space Group) Calculated from XRD Patterns

	pristine material			delithiated material		
	a , Å	c , Å	V , Å ³	a , Å	c , Å	V , Å ³
NMC111	2.858	14.222	100.58	2.820	14.339	98.79
NMC532	2.872	14.249	101.79	2.821	14.186	97.76
NMC622	2.868	14.211	101.24	2.817	14.074	96.75
NMC811	2.871	14.205	101.38	2.814	14.108	96.77

for all of the calculations. Hence, the only difference between calculations was the composition and therefore the chemical environment of the transition metal to be dissolved.

The formation energies of the biacetyl complexes, ML_3^{n+} (where L = biacetyl), are shown in Tables 6 and 7. We computed values of the formation energies of the ML_3^{n+} complexes, assuming that the complex could form on several

Table 5. Average Concentrations of Metals in Solution^a

positive electrode material	average concentration without biacetyl present, μM			average concentration with biacetyl present, μM		
	Mn	Co	Ni	Mn	Co	Ni
NMC111	9.56×10^{-2} (2.36×10^{-2})	1.65×10^{-2} (1.39×10^{-2})	4.96×10^{-2} (1.39×10^{-3})	3.77×10^{-1} (6.16×10^{-1})	1.04×10^{-1} (1.96×10^{-1})	1.30 (1.35×10^{-1})
NMC532	7.94×10^{-2} (2.18×10^{-3})	1.36×10^{-2} (1.36×10^{-3})	1.32×10^{-1} (6.00×10^{-2})	1.07×10^{-1} (6.60×10^{-1})	3.18×10^{-2} (3.25×10^{-2})	1.00 (6.18×10^{-1})
NMC622	1.18×10^{-1} (8.59×10^{-2})	1.82×10^{-1} (1.78×10^{-1})	1.37×10^{-1} (5.49×10^{-2})	1.49×10^{-1} (5.66×10^{-1})	2.71×10^{-1} (1.31×10^{-1})	5.64×10^{-1} (7.20×10^{-1})
NMC811	4.50×10^{-2} (2.24×10^{-2})	2.71×10^{-2} (2.71×10^{-3})	1.41×10^{-1} (5.26×10^{-2})	6.96×10^{-2} (5.65×10^{-2})	2.71×10^{-2} (7.33×10^{-6})	1.33×10^{-1} (9.61×10^{-2})

^aThe number in parentheses represents the uncertainty in the measurement (1σ).

Table 6. Biacetyl–Metal Complex Formation Energy with Metal Dissolved from the Surface (104)

positive electrode material	formation energy (kJ/mol)		
	Mn	Co	Ni
NMC111	−9.62	−19.2	−76.8
NMC532	−28.83	−8.64	−48.0
NMC622	−86.40	−6.79	−10.56
NMC811	−76.41	−6.53	−10.21

Table 7. Biacetyl–Metal Complex Formation Energy with Metal Dissolved from the Surface (012)

positive electrode material	formation energy (kJ/mol)		
	Mn	Co	Ni
NMC111	−16.3	−20.40	−87.1
NMC532	−33.4	−10.72	−64.2
NMC622	−76.2	−8.40	−33.9
NMC811	−62.1	−7.32	−25.8

surfaces (i.e., facets of the $\text{Li}(\text{Ni,Mn,Co})\text{O}_2$ crystal). The formation energy was computed as the energy difference ($\Delta_f E$) between the slab model with the metal at the surface (E_{surf}) and the slab model with the dissolved metal complexed by biacetyl (E_{complex}): $\Delta_f E = E_{\text{complex}} - E_{\text{surf}}$. The DFT calculations predict that Ni would be more easily extracted by biacetyl in NMC111. The formation energy of the complex in that composition becomes less negative when the content of Ni in the material increases. This behavior matches the experimental results where the Ni concentration in solution decreases when the Ni content increases in the positive electrode.

Since the concentrations of manganese and cobalt in Table 5 were effectively zero, the corresponding values in Tables 6 and 7 were not used further. Additionally, the concentrations of nickel in solution from NMC622 and NMC811 were assumed to be zero.

Plotting the formation energies shown in Tables 6 and 7 as a function of the concentration of nickel (Figure 6) shows similar trends to the experimental data. Data from both the (012) and (104) surfaces show that the formation energy of nickel–biacetyl complex tends to become more negative as the amount of nickel in the solid decreases. This correlation suggests that something disfavors complex formation at high X_{Ni} in the solid. That is, nickel is becoming more stable in the surface lattice at high X_{Ni} . In fact, our DFT results show that NMC111 and NMC532 have enough transition-metal sites (Co^{3+} and Ni^{3+}) near the dissolution site that can be oxidized as a result of Ni dissolution. That is, for example, if Ni^{3+} disproportionates into Ni^{2+} and Ni^{4+} , Ni^{2+} can dissolve in the electrolyte. However, in NMC811, all of the atoms (mostly Ni) near the dissolution site are in the 4+ oxidation state. The absence of nearby transition metals that can accommodate the two holes left by the dissolving transition metal reduces the formation energy of transition-metal vacancies. The next available sites are further away and need to be electronically accessible. In fact, the band gap of NiO_2 is shown to be higher than that for LiNiO_2 , while the reverse ordering is true for CoO_2 vs LiCoO_2 .³³ This suggests that lower Co concentrations near the dissolution site reduce material conductivity, enhancing the effect of local configurations on the accessibility to higher oxidation states. Of course, for Ni-rich compositions (NMC811) in high charge states, the NiO-like rock salt phase

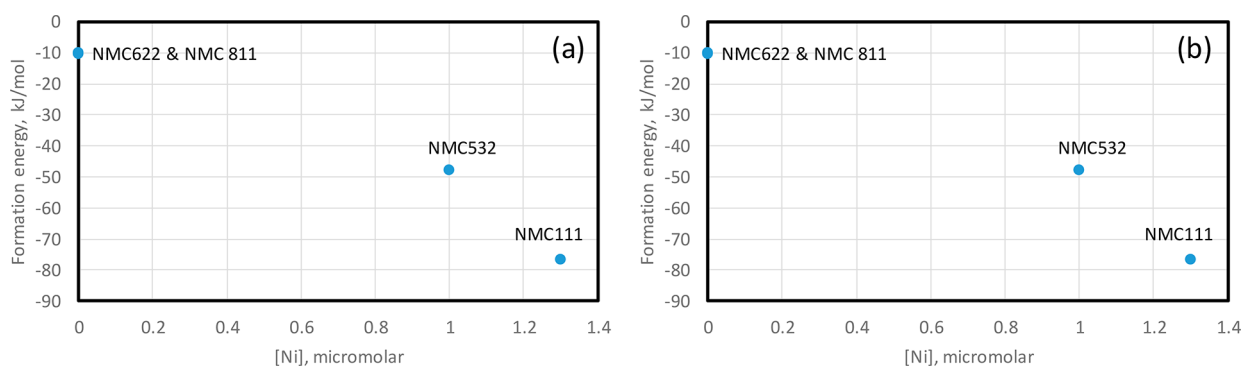


Figure 6. Calculated formation energies of Ni-biacetyl complexes vs the observed nickel concentration for the oxides studied: (a) the (104) surface and (b) the (012) surface.

Table 8. Concentrations of Transition Metals in Solution^a

positive electrode material	concentration without bifluoride present, μM				concentration with bifluoride present, μM			
	F	Mn	Co	Ni	F	Mn	Co	Ni
NMC111	3.68×10^{-2} (3.16×10^{-3})	0.07 (0.02)	0.02 (0.02)	0.05 (0.005)	215.31 (102.45) ^b	20.03 (8.93)	7.78 (2.16)	4.11 (0.59)
NMCS32	0.00	0.07 (0.10)	0.35 (0.56)	0.06 (0.03)	4.42×10^5 (1.99×10^5)	15.57 (4.44)	3.63 (1.02)	5.53 (0.91)
NMC622	203.26 (357.77)	0.14 (0.08)	0.02 (0.002)	0.40 (0.47)	1.99×10^5 (8.43×10^4)	25.06 (8.42)	4.24 (1.21)	10.37 (2.19)
NMC811	137.09 (48.25)	0.03 (0.03)	0.01 (0.001)	0.11 (0.01)	1.44×10^5 (2.98×10^4)	11.95 (5.02)	1.23 (0.52)	11.30 (3.62)

^aThe number in parentheses represents the uncertainty in the measurement (1σ). ^bLarge standard deviation values are due to the method used to add the bifluoride.

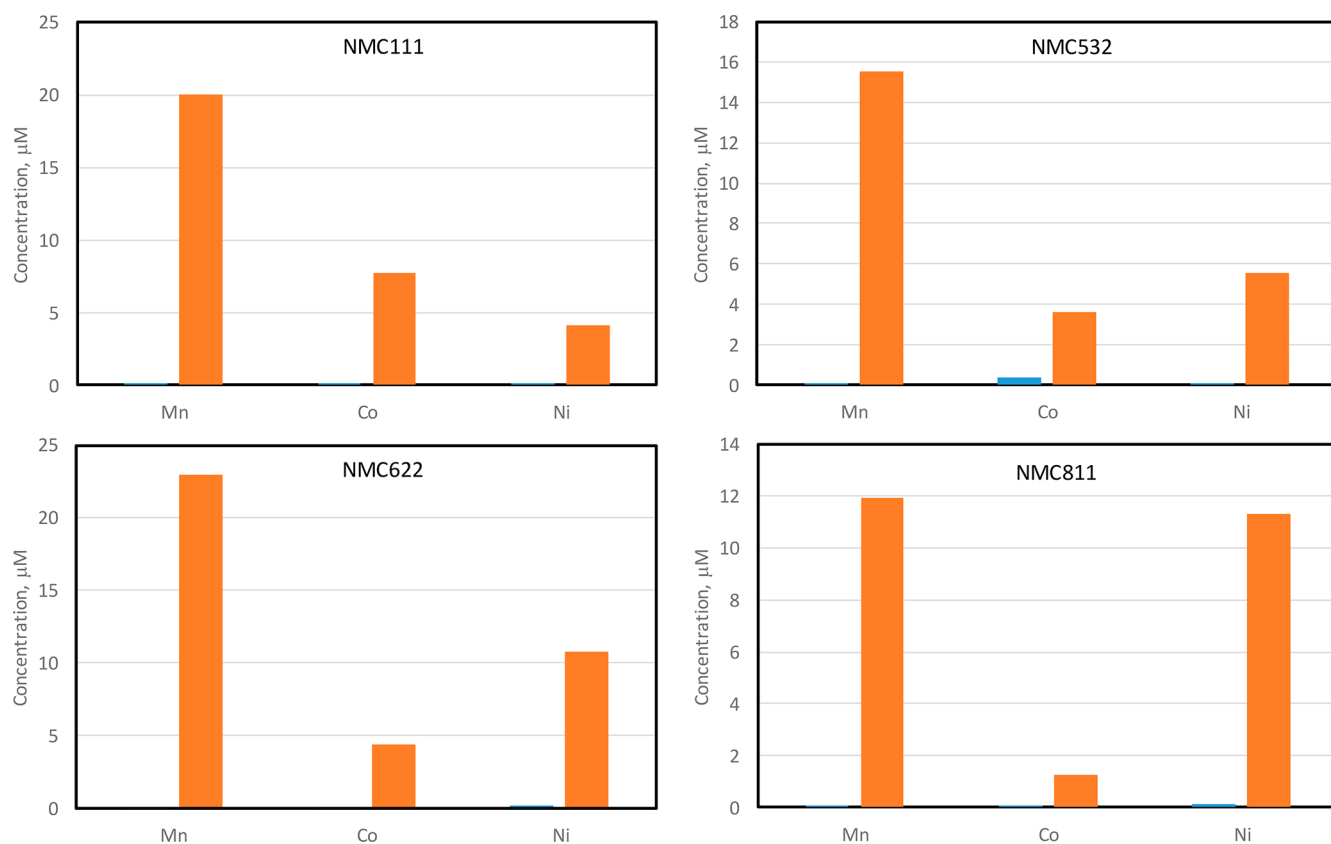


Figure 7. Concentrations of manganese, cobalt, and nickel in solution from the positive electrode materials used in this study. The concentrations of the metals without the additive are given as blue bars, and with it, as orange ones. Due to the large differences in the relative concentrations, the blue bar is not visible in all plots.

might form at the surface. Such a phase is, in fact, very stable with respect to dissolution.

3.2. Bifluoride. Table 8 shows concentrations of the transition metals with and without the addition of bifluoride. From these data, the concentrations of the transition metals in the absence of bifluoride are practically zero. At face value, one concentration of cobalt seems excessively high. However, when the uncertainty in this value is considered, it is the same as the others, practically zero.

Bifluoride was always present in excess, as shown in Table 8, so that it would not be considered a limiting reagent in the leaching process. As can be seen from the two sides of the table, bifluoride produced a large change in the concentrations of Mn, Co, and Ni. These data are plotted in Figure 7.

The relative changes ($[\text{metal with additive}] - [\text{metal without additive}]/[\text{metal without additive}]$) were calculated from these values and are shown in Table 9. The concentrations of manganese and cobalt in solution showed the largest change, in general, in response to the addition of bifluoride.

Table 9. Relative Change in Concentration Caused by Bifluoride Addition

positive electrode material	relative change		
	[Mn]	[Co]	[Ni]
NMC111	272.93	515.78	90.45
NMC532	221.18	10.52	90.23
NMC622	214.71	296.66	50.40
NMC811	345.04	90.67	98.33

The results of the fitting exercise showed that no combinations of the terms in eq 6 made both chemical and statistical sense when no bifluoride was present. Even though four combinations were identified using X_{Mn} and X_{Co} for [Co], plotting them showed that these results amounted to fitting just two points. The results were of the form $(X_{\text{Mn}})^n(X_{\text{Co}})^m$, where n and m were either -1 or -2 . For example, when $m = 1$ and $n = -1$, there were just two unique points, 1 and 1.5, rendering the “overdetermined” fitting result invalid. Other combinations of m and n produced different values but led to the same conclusion.

When bifluoride was present, the search algorithm and selection criteria generated 19 possibilities. These were further limited by looking for an expression where the sum of the exponents was the smallest, implying simpler contributions from the metal(s) to the corrosion process, making the metal(s) soluble in the electrolyte. That is, an expression, such as X_{Co} (sum of exponents = 1), was chosen over $(X_{\text{Co}})^2(X_{\text{Ni}})$ (sum = 3) because the former implied that just cobalt was involved and not two metals. Four possibilities were thus chosen from the original 19 and are plotted in Figure 8. There were two for [Ni] and one each for [Mn] and [Co]. From the values of r^2 given in the figure caption, the fits were very good.

In most cases, the relationships showed that the concentration of the transition metals increased with the expression given on the x axis of the charts in Figure 8. The plots show that [Mn] increased with $X_{\text{Ni}}X_{\text{Co}}$; [Ni], with $X_{\text{Co}}(X_{\text{Ni}})^3$; and [Co], with X_{Co} . However, we did find that, as $(X_{\text{Mn}})^2$ increased, [Ni] decreased.

No atomistic modeling results were available. The system was too complex for the calculations to readily converge.

4. DISCUSSION

In the geology and hydrometallurgy literature, there are many reports of species-assisted dissolution or leaching of metals from oxides, sulfides, and silicates in aqueous media.^{34–42} For example, the dissolution of lead and zinc from low-grade sulfide ore in alkaline solutions was found to be sensitive to the concentration of sodium hydroxide.³⁷ In another study, the dissolution rate of uranium from UTi_2O_6 in aqueous $\text{H}_2\text{SO}_4/\text{Fe}_2(\text{SO}_4)_3$ solutions was found to depend on the concentration of $\text{Fe}_2(\text{SO}_4)_3$, while the dissolution of titanium depended on the acid concentration. Gilligan et al.³⁸ proposed that the reaction proceeded by the oxidation and dissolution of uranium to form a soluble $\text{UO}_2(\text{SO}_4)_2^{2-}$ species, which left a titanium-rich surface that was subsequently attacked by acid.

Organic acids, such as citric and gluconic acids, have also been used to leach metals from ores. Although these acids have limited leaching ability, they were used because they offer greater selectivity.^{39–41}

Given the above, the dissolution of transition metals in the battery electrolyte can be thought of as a leaching process. We analyzed and interpreted our results, building on some of the concepts from the above references. In its simplest form, the general leaching reaction for a given positive electrode material can be written as $\text{Li}_{1-x}\text{MO}_2(\text{s}) + \text{Z}(\text{solution}) \rightarrow \alpha\text{MZ}(\text{solution}) + \text{Li}_{1-x}\text{M}_{1-\alpha}\text{O}_2(\text{s})$, where M represents the transition metals in the positive electrode; $\text{Li}_{1-x}\text{MO}_2$, the delithiated positive electrode material; Z, the leaching agent, such as biacetyl or bifluoride; and MZ, the product of the leaching reaction.

According to Stumm and Wollast,⁴² the rate law for the chemical weathering of rocks (i.e., leaching of metals) by a surface-controlled reaction is generally given as $R = kC_j$, where R is the observed dissolution rate of a metal, k is a rate constant, and C_j is proportional to the surface concentration of species j that are chemically reactive. Possible reacting surface species are shown in Figure 9.

The knowledge obtained from the leaching of metals during the weathering of rocks and of other materials in aqueous solutions can serve as a good starting point for understanding the dissolution process in lithium-ion battery cathodes. In an aqueous-based system, there are two possible species that can react with the surface, H^+ and HO^- . As one changes the pH, the concentration of these species changes. At low pH, H^+ would be the major contributor to the leaching reaction. At pH 7, they would contribute “equally.” At high pH, HO^- would be the main leaching agent. Therefore, the mechanism can change with pH.

However, the usual concept of pH does not apply to nonaqueous systems; therefore, this situation is not present in the static reactions described in our work. The leaching agents in our work are H^+ and F^- . The concentration of these species does not vary as in the case of water, where one increases at the expense of the other. Instead, both $[\text{H}^+]$ and $[\text{F}^-]$ increase simultaneously with the addition of the bifluoride, and the leaching mechanism would not be expected to change.

In most surface-mediated reactions, the reaction rate is controlled by the amount of reactants available and by mass transport. If we consider the cathode surface to be the limiting reactant, then it should not matter how much bifluoride is present. The reaction will proceed at its limiting rate at the reaction temperature.

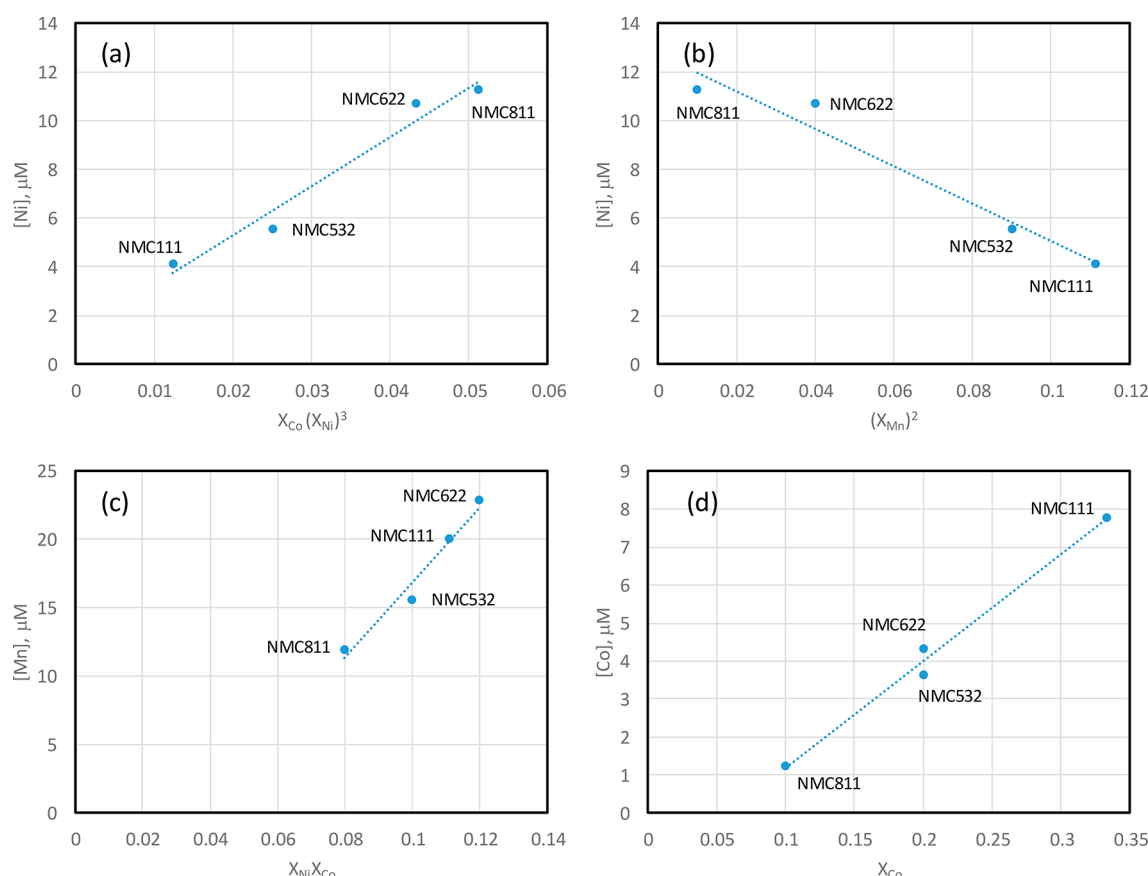


Figure 8. Concentrations of the transition metals vs various combinations of the ideal stoichiometries with bifluoride present. Markers represent the data, and dotted lines, the least-squares fit. The regression yielded the following equations (value of r^2): (a) $[\text{Ni}] = 203.07X_{\text{Co}}(X_{\text{Ni}})^3 + 1.23$ (0.97); (b) $[\text{Ni}] = -77.04(X_{\text{Mn}})^2 + 12.76$ (0.96); (c) $[\text{Mn}] = 275.67X_{\text{Co}}(X_{\text{Ni}}) - 10.71$ (0.97); and (d) $[\text{Co}] = 28.09X_{\text{Co}} - 1.61$ (0.99).

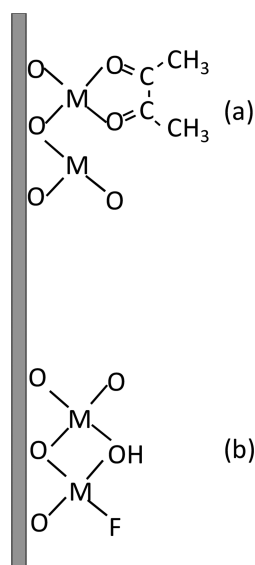


Figure 9. Possible surface species formed with the leaching agent: (a) biacetyl and (b) bifluoride.

If C_j is proportional to mole fraction X_M (where M is Ni, Mn, or Co), then applying this last expression to the NMC oxides yields the expression $R = k'X_M$. The possibility that R is not first order in X_M can be easily handled by using the principles of equilibrium kinetics, that is, $R = k''X_M^\alpha$, where α is an integer between -5 and 5 . If $\alpha < 0$, then X_M retards the rate

of reaction; if $\alpha > 0$, then X_M increases the rate of reaction. Extending this idea to include the possibility of contributions from the other metals in the positive electrode to either retard or accelerate the dissolution reaction produces $R = k'''X_{\text{Ni}}^\alpha X_{\text{Mn}}^\beta X_{\text{Co}}^\gamma$, where β and γ have the same restrictions as α . At a fixed Δt interval, the rate expression becomes eq 6.

As might be expected, in general, the effect of the fluoride-containing leaching agent was larger than that observed from biacetyl. The bifluoride typically caused between ~ 4 and ~ 170 times as much metal dissolution from the positive electrode materials. In the case of Ni from NMC111 and NMC532, for which biacetyl showed the most significant dissolution, the effect (~ 4 - or 5 -fold) was on the lower end of the range seen with bifluoride. When biacetyl was the leaching agent, however, $[\text{Ni}]$ did not follow the trend related to the increasing nickel fraction in NMC111, NMC532, NMC622, and NMC811. The fact that the observed $[\text{Ni}]$ in solution effectively drops to zero in the case of NMC622 and NMC811 might indicate that the surface chemistry of the positive electrode plays an important part in the leaching process.

Taking the fitting results for Ni as an example, the two expressions state that $[\text{Ni}]$ is proportional to $X_{\text{Co}}(X_{\text{Ni}})^3$ and is inversely proportional to $(X_{\text{Mn}})^2$. These expressions can be related to possible configurations of atoms on the surface of the charged positive electrode. For example, if one considers the arrangements of next-nearest neighbors (NNNs) around a central Ni atom, then the schematics shown in Figure 10 are possible. The configuration in A, in which three other nickel atoms are NNNs, would be more favorable to dissolution than

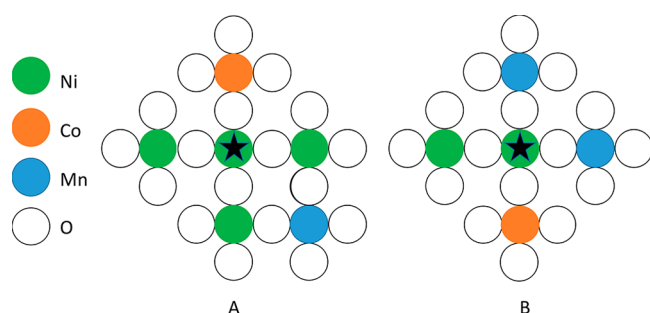


Figure 10. Schematics of two configurations of the surface of the NMC oxides. The star indicates the Ni atom of interest. Configuration A speeds up Ni dissolution. Configuration B slows it down.

the configuration shown in B, in which only two other nickel atoms are NNNs. On the basis of the principles outlined above, configuration B (and its associated rate law) would still accelerate the dissolution process; the value of the exponent of X_{Mn} in the rate law is positive (see Figure 7). However, the fitting results yielded a negative fitting coefficient for $(X_{\text{Mn}})^2$, the opposite of expectation, implying that there may be more to the leaching process than the ideas outlined above.

Comparing the results from biacetyl and bifluoride shows that the leaching process may depend on factors other than the configuration of atoms on the surface of the particle. The leaching process may be affected by lattice stabilization due to the NNNs and by the free energy (and kinetics) of formation of the transition-metal-containing product in solution. The free energies of formation of the leached product are probably not similar, so the configurations of surface atoms imparting stability are also not similar.

5. CONCLUSIONS

The response of charged, positive electrode materials in the $\text{Li}(\text{Mn}, \text{Ni}, \text{Co})\text{O}_2$ family was tested experimentally by using two leaching agents, biacetyl and bifluoride, in static tests. These agents represent species that might be found in an operating lithium-ion cell and that may be responsible for the increased rate of corrosion at high voltages. The response to biacetyl was statistically weak, but it was more selective for Ni than for the other metals, as expected. The response to the bifluoride salt was statistically stronger, allowing for modeling of the process. We found that $[\text{Ni}]$ was proportional to $X_{\text{Co}}(X_{\text{Ni}})^3$ and inversely proportional to $(X_{\text{Mn}})^2$; $[\text{Mn}]$ to $X_{\text{Co}}(X_{\text{Ni}})$; and $[\text{Co}]$ to X_{Co} , which suggests that nickel as a next-nearest neighbor can make dissolution more favorable in some instances. These expressions can be related to possible configurations of atoms on the surface of the charged positive electrode. Different de/stabilizing NNN configurations were found for the two leaching agents, implying that the free energy of formation of the product should also be included.

AUTHOR INFORMATION

Corresponding Author

Ira Bloom – Chemical Sciences and Engineering Division, Argonne National Laboratory, Lemont, Illinois 60439, United States; orcid.org/0000-0002-4877-473X; Phone: 630-252-4516; Email: ira.bloom@anl.gov

Authors

Hannah R. Morin – Chemical Sciences and Engineering Division, Argonne National Laboratory, Lemont, Illinois 60439, United States; Department of Chemistry, The University of Chicago, Chicago, Illinois 60637, United States

Donald G. Graczyk – Analytical Chemistry Laboratory, Chemical and Fuel Cycle Technologies Division, Argonne National Laboratory, Lemont, Illinois 60439, United States

Yifen Tsai – Analytical Chemistry Laboratory, Chemical and Fuel Cycle Technologies Division, Argonne National Laboratory, Lemont, Illinois 60439, United States

Susan Lopykinski – Analytical Chemistry Laboratory, Chemical and Fuel Cycle Technologies Division, Argonne National Laboratory, Lemont, Illinois 60439, United States

Hakim Iddir – Chemical Sciences and Engineering Division, Argonne National Laboratory, Lemont, Illinois 60439, United States; orcid.org/0000-0001-5285-6474

Juan C. Garcia – Chemical Sciences and Engineering Division, Argonne National Laboratory, Lemont, Illinois 60439, United States; orcid.org/0000-0002-5911-8850

Nancy Dietz Rago – Chemical Sciences and Engineering Division, Argonne National Laboratory, Lemont, Illinois 60439, United States

Stephen Trask – Chemical Sciences and Engineering Division, Argonne National Laboratory, Lemont, Illinois 60439, United States

LeRoy Flores – Chemical Sciences and Engineering Division, Argonne National Laboratory, Lemont, Illinois 60439, United States

Seoung-Bum Son – Chemical Sciences and Engineering Division, Argonne National Laboratory, Lemont, Illinois 60439, United States

Zhengcheng Zhang – Chemical Sciences and Engineering Division, Argonne National Laboratory, Lemont, Illinois 60439, United States; orcid.org/0000-0002-0467-5801

Noah M. Johnson – Chemical Sciences and Engineering Division, Argonne National Laboratory, Lemont, Illinois 60439, United States

Complete contact information is available at:

<https://pubs.acs.org/10.1021/acsaem.9b02277>

Notes

The authors declare no competing financial interest.

ACKNOWLEDGMENTS

We gratefully acknowledge support from the U.S. Department of Energy (DOE), Vehicle Technologies Office, specifically from Peter Faguy and David Howell. Argonne National Laboratory is operated for the DOE Office of Science by UChicago Argonne, LLC, under contract number DE-AC02-06CH11357. The electrodes used in this article were made by Argonne's Cell Analysis, Modeling and Prototyping (CAMP) Facility, which was supported by the Applied Battery Research for Transportation Program. The U.S. government retains for itself, and others acting on its behalf, a paid-up nonexclusive, irrevocable worldwide license in said article to reproduce, prepare derivative works, distribute copies to the public, and perform publicly and display publicly by or on behalf of the government.

REFERENCES

- (1) Terborg, L.; Weber, S.; Blaske, F.; Passerini, S.; Winter, M.; Karst, U.; Nowak, S. Investigation of thermal aging and hydrolysis mechanisms in commercial lithium battery electrolyte. *J. Power Sources* **2013**, *242*, 832–837.
- (2) Faenza, N. V.; Lebens-Higgins, Z. W.; Mukherjee, P.; Sallis, S.; Pereira, N.; Badway, F.; Halajko, A.; Ceder, G.; Cosandey, V.; Piper, L. F. J.; Amatucci, G. G. Electrolyte-induced surface transformation and transition-metal dissolution of fully delithiated $\text{Li-Ni}_{0.8}\text{Co}_{0.15}\text{Al}_{0.05}\text{O}_2$. *Langmuir* **2017**, *33*, 9333–9353.
- (3) Hunter, J. C. Preparation of a new crystalline form of manganese dioxide: $\lambda\text{-MnO}_2$. *J. Solid State Chem.* **1981**, *39*, 142–147.
- (4) Gummow, R. J.; de Kock, A.; Thackeray, M. M. Improved capacity retention in rechargeable 4 V lithium/lithium manganese oxide (spinel) cells. *Solid State Ionics* **1994**, *69*, 59–67.
- (5) Jang, D. H.; Shin, Y. J.; Oh, S. M. Dissolution of spinel oxides and capacity losses in 4 V $\text{Li/Li}_x\text{Mn}_2\text{O}_4$ cells. *J. Electrochem. Soc.* **1996**, *143*, 2204–2211.
- (6) Zhan, C.; Wu, T.; Lu, J.; Amine, K. Dissolution, migration, and deposition of transition metal ions in Li-ion batteries exemplified by Mn-based cathodes – a critical review. *Energy Environ. Sci.* **2018**, *11*, 243–257.
- (7) Pieczonka, N. P. W.; Liu, Z.; Lu, P.; Olson, K. L.; Moote, J.; Powell, B. R.; Kim, J.-H. Understanding transition-metal dissolution behavior in $\text{LiNi}_{0.5}\text{Mn}_{1.5}\text{O}_4$ high-voltage spinel for lithium ion batteries. *J. Phys. Chem. C* **2013**, *117*, 15947–15957.
- (8) Wohlfahrt-Mehrens, M.; Vogler, C.; Garche, J. Aging mechanisms of lithium cathode materials. *J. Power Sources* **2004**, *127*, 58–64.
- (9) Zheng, H.; Sun, Q.; Liu, G.; Song, X.; Battaglia, V. S. Correlation between dissolution behavior and electrochemical cycling performance for $\text{LiNi}_{1/3}\text{Co}_{1/3}\text{Mn}_{1/3}\text{O}_2$ -based cells. *J. Power Sources* **2012**, *207*, 134–140.
- (10) Bhandari, A.; Bhattacharyaz, J. Review—Manganese dissolution from spinel cathode: Few unanswered questions. *J. Electrochem. Soc.* **2017**, *164*, A106–A127.
- (11) Aoshima, T.; Okahara, K.; Kiyohara, C.; Shizuka, K. Mechanisms of manganese spinel dissolution and capacity fade at high temperature. *J. Power Sources* **2001**, *97–98*, 377–380.
- (12) Gallus, D. R.; Schmitz, R.; Wagner, R.; Hoffmann, B.; Nowak, S.; Cekic-Laskovic, I.; Winter, M. The influence of different conducting salts on the metal dissolution and capacity fading of NCM cathode material. *Electrochim. Acta* **2014**, *134*, 393–398.
- (13) Jarry, A.; Gottis, S.; Yu, Y.-S.; Roque-Rosell, J.; Kim, C.; Cabana, J.; Kerr, J.; Kostecki, R. The formation mechanism of fluorescent metal complexes at the $\text{Li}_x\text{Ni}_{0.5}\text{Mn}_{1.5}\text{O}_{4-\delta}$ /carbonate ester electrolyte interface. *J. Am. Chem. Soc.* **2015**, *137*, 3533–3539.
- (14) Gilbert, J. A.; Shkrob, I. A.; Abraham, D. P. Transition metal dissolution, ion migration, electrocatalytic reduction and capacity loss in lithium-ion full cells. *J. Electrochem. Soc.* **2017**, *164*, A389–A399.
- (15) Structures were rendered using PerkinElmer Chem3D Pro 18.1 and the online ChemACX library.
- (16) Anhydrous ethylene glycol was not available commercially, and glyoxal is usually found as a polymer.
- (17) Brunck, O. Über die Anwendung des Dimethylglyoxims zur Bestimmung des Nickels und zu seiner Trennung von den Metallen der Schwefelammoniumgruppe. *Angew. Chem.* **1907**, *20*, 1844–1850.
- (18) Tschugäff, L. Über ein neues empfindliches Reagens auf Nickel. *Ber. Dtsch. Chem. Ges.* **1905**, *38*, 2520–2522.
- (19) Holm, E.; Roos, P.; Skwarzec, B. Radioanalytical studies of fallout ^{63}Ni . *Appl. Radiat. Isol.* **1992**, *43*, 371–376.
- (20) Chen, X.; Zhou, T.; Kong, J.; Fang, H.; Chen, Y. Separation and recovery of metal values from leach liquor of waste lithium nickel cobalt manganese oxide-based cathodes. *Sep. Purif. Technol.* **2015**, *141*, 76–83.
- (21) Cell Analysis, Modeling and Prototyping.
- (22) Toby, B. H.; Von Dreele, R. B. GSAS-II: the genesis of a modern open-source all purpose crystallography software package. *J. Appl. Crystallogr.* **2013**, *46*, 544–549.
- (23) Kresse, G.; Furthmüller, J. Efficiency of ab-initio total energy calculations for metals and semiconductors using a plane-wave basis set. *Comput. Mater. Sci.* **1996**, *6*, 15–50.
- (24) Kresse, G.; Hafner, J. Ab initio molecular dynamics for liquid metals. *Phys. Rev. B: Condens. Matter Mater. Phys.* **1993**, *47*, 558–561.
- (25) Perdew, J. P.; Burke, K.; Ernzerhof, M. Generalized gradient approximation made simple. *Phys. Rev. Lett.* **1996**, *77*, 3865–3868.
- (26) Blöchl, P. E. Projector augmented-wave method. *Phys. Rev. B: Condens. Matter Mater. Phys.* **1994**, *50*, 17953–17979.
- (27) Garcia, J. C.; Bareño, J.; Yan, J.; Chen, G.; Hauser, A.; Croy, J. R.; Iddir, H. Surface structure, morphology, and stability of $\text{Li}(\text{Ni}_{1/3}\text{Mn}_{1/3}\text{Co}_{1/3})\text{O}_2$ cathode material. *J. Phys. Chem. C* **2017**, *121*, 8290.
- (28) Mathew, K.; Sundaraman, R.; Letchworth-Weaver, K.; Arias, T. A.; Hennig, R. G. Implicit solvation model for density-functional study of nanocrystal surfaces and reaction pathways. *J. Chem. Phys.* **2014**, *140*, 084106.
- (29) Mathew, K.; Hennig, R. G. Implicit self-consistent description of electrolyte in plane-wave density-functional theory. *ArXiv1601.03346*, 2016.
- (30) Hall, D. S.; Self, J.; Dahn, J. R. Dielectric constants for quantum chemistry and Li-ion batteries: Solvent blends of ethylene carbonate and ethyl methyl carbonate. *J. Phys. Chem. C* **2015**, *119*, 22322–22330.
- (31) Ryu, H.-H.; Park, K.-J.; Yoon, C. S.; Sun, Y.-K. Capacity fading of Ni-rich $\text{Li}[\text{Ni}_x\text{Co}_y\text{Mn}_{1-x-y}]\text{O}_2$ ($0.6 \leq x \leq 0.95$) cathodes for high-energy-density lithium-ion batteries: Bulk or surface degradation? *Chem. Mater.* **2018**, *30*, 1155–1163.
- (32) Kim, J.-H.; Ryu, H.-H.; Kim, S. J.; Yoon, C. S.; Sun, Y.-K. Degradation mechanism of highly Ni-rich $\text{Li}[\text{Ni}_x\text{Co}_y\text{Mn}_{1-x-y}]\text{O}_2$ cathodes with $x > 0.9$. *ACS Appl. Mater. Interfaces* **2019**, *11*, 34.
- (33) Seo, D.-H.; Urban, A.; Ceder, G. Calibrating transition-metal energy levels and oxygen bands in first-principles calculations: Accurate prediction of redox potentials and charge transfer in lithium transition-metal oxides. *Phys. Rev. B: Condens. Matter Mater. Phys.* **2015**, *92* (2015), 115118.
- (34) Terry, B. Specific chemical rate constants for the acid dissolution of oxides and silicates. *Hydrometallurgy* **1983**, *11*, 315–344.
- (35) Crundwell, F. The mechanism of dissolution of minerals in acidic and alkaline solutions: Part I: A new theory of non-oxidation dissolution. *Hydrometallurgy* **2014**, *149*, 252–264.
- (36) Crundwell, F. The mechanism of dissolution of minerals in acidic and alkaline solutions: Part III. Application to oxide, hydroxide and sulfide minerals. *Hydrometallurgy* **2014**, *149*, 71–81.
- (37) Ghasemi, S. M. S.; Azizi, A. J. Alkaline leaching of lead and zinc by sodium hydroxide: kinetics modeling. *J. Mater. Res. Technol.* **2018**, *7*, 118–125.
- (38) Gilligan, R.; Nioloski, A. N. Leaching of brannerite in the ferric sulphate system – Part I. Kinetics and reaction mechanisms. *Hydrometallurgy* **2015**, *156*, 71–80.
- (39) Hurşit, M.; Laçin, O.; Saraç, H. Dissolution kinetics of smithsonite ore as an alternative zinc source with an organic leach agent. *J. Taiwan Inst. Chem. Eng.* **2009**, *40*, 6–12.
- (40) Larba, R.; Boukerche, I.; Alane, N.; Habbache, N.; Djerad, S.; Tifouti, L. Citric acid as an alternative lixiviant for zinc oxide dissolution. *Hydrometallurgy* **2013**, *134–135*, 117–123.
- (41) Wu, D. D.; Wen, S. M.; Yang, J.; Deng, J. S. Investigation of dissolution kinetics of zinc from smithsonite in 5-sulphosalicylic acid. *Can. Metall. Q.* **2015**, *54*, 51–57.
- (42) Stumm, W.; Wollast, R. Coordination chemistry of weathering: Kinetics of the surface-controlled dissolution of oxide minerals. *Rev. Geophys.* **1990**, *28*, 53–69.